

Seeing Double: Transient Dips and Photometric Binarity in PTFO 8-8695

L. G. BOUMA¹ AND J. N. WINN¹

¹ *Department of Astrophysical Sciences, Princeton University, 4 Ivy Lane, Princeton, NJ 08540, USA*

(Received April 23, 2020; Revised —; Accepted —)

Submitted to AAS journals.

ABSTRACT

PTFO 8-8695b is a candidate hot Jupiter in the 7–10 million year old Orion-OB1a cluster. We inspected data from TESS and Gaia to clarify whether it is truly a planet. The Gaia data show that PTFO 8-8695 is a photometric binary with respect to members of its kinematic group, and independently suggest that it is an astrometric binary. The TESS lightcurve shows that the dominant variability in this system is sinusoidal with a long period $P_\ell = 11.96$ hr, presumably caused by stellar rotation. Also present is a combined dip and asymmetric sinusoid, previously identified as the planet candidate, that repeats with a short period $P_s = 10.74$ hr. The two signals beat every 4.48 days. Although there is a dip in the short-period signal, ground-based photometry from the past decade indicates that the orbital phase of the dip seems to have instantaneously jumped, at least once, and perhaps twice. Planets do not “jump” in orbital phase. Given the available evidence, we believe that PTFO 8-8695 is a binary M dwarf in which one star shows the long rotation signal, and the other star shows transient dipping that has been seen in a few other young low-mass stars. The origin of these transient dips is still undetermined.

Keywords: Exoplanet evolution (491), Pre-main sequence stars (1290), Stellar ages (1581), Stellar rotation (1629), Variable stars (1761), Low mass stars (2050)

1. INTRODUCTION

If PTFO 8-8695b were a planet, it would be exceptional. At below 10 million years of age, it could be the youngest hot Jupiter known (van Eyken et al. 2012). Its orbital period of only 10.7 hours around a weak-lined T Tauri M dwarf would also give it the shortest period of any known hot Jupiter. With such a short period, it would almost certainly have filled its Roche lobe, and would be actively losing mass to its host star. Not only that, but the rapidly rotating host star would also be oblate and gravity darkened, and so the planet’s orbit would likely precess into and out of transitability (Barnes et al. 2013; Ciardi et al. 2015; Kamiaka et al. 2015).

Other lines of evidence would imply further planetary “firsts” for this planet candidate. One first would be that its transits are about three times deeper in optical band-passes (e.g., *g*-band) than in the near-infrared (e.g., *z*-band) (Onitsuka et al. 2017; Tanimoto et al. 2020). A cloud-free hydrogen-dominated planetary atmosphere cannot explain such a wavelength dependence. The planet might therefore be surrounded by a dust cloud (Tanimoto et al. 2020).

Another first could be the direct detection of H α emission from the planet itself (Johns-Krull et al. 2016). While the stellar chromosphere emits in H α , it seems that there is an additional excess H α emission that could be in phase with the planetary orbit. The average velocity width of the excess H α emission is 87 km s^{−1}, and its equivalent width is 70–80% that of the stellar chromosphere (Johns-Krull et al. 2016). The proposed explanation is that outflowing mass from the planet could explain this excess emission as well (Johns-Krull et al. 2016).

There are perhaps a few challenges to the planetary interpretation (if these “features” are not already seen as such). They include that the planet does not seem to emit infrared radiation in occultation, at least at the expected amplitude (Yu et al. 2015). In addition, despite measurement attempts by multiple investigators, PTFO 8-8695b does not seem to show the Rossiter effect at the amplitude expected given the rapid stellar rotation and large planet size (Yu et al. 2015; Ciardi et al. 2015). Finally, detailed modelling of the “precession + gravity darkening” transits has shown that the necessary degree of gravity darkening is too great, given the spectroscopically observed equatorial velocity (Howarth 2016). Additionally, as the gravity-darkened star precessed about its rotation axis, it would need to show photometric variability that has not been observed.

While the planetary interpretation clearly faces challenges, alternative explanations do as well. High-latitude accretion hotspots might produce the observed $H\alpha$ variability, but require fine-tuning to produce dips of the appropriate duration. Furthermore, PTFO 8-8695 does not have an infrared (IR) excess associated with the presence of dust at the inner edge of a primordial disk (*e.g.*, Yu et al. 2015, Figure 18). Low-latitude starspots, hot or cold, struggle to produce the necessary dip durations.

One potentially relevant fact is that between 0.1% and 1% of rapidly rotating low-mass stars in $\mathcal{O}(10)$ Myr old associations show narrow dips in phase with strong stellar rotation signals (Rebull et al. 2018). The dips can persist over months, but their depths often vary, and sometimes change immediately after stellar flares. The explanation proposed by Stauffer et al. (2017) and David et al. (2017) to explain this novel class of variable stars is that a circumstellar cloud of gas might be orbiting near the Keplerian co-rotation radius. To date, this explanation has not clearly been viable for PTFO 8-8695, because a clear determination of the stellar rotation period has not yet been possible (van Eyken et al. 2012; Koen 2015; Rietz et al. 2016).

We begin in Section 2 by describing newly available observations from TESS (Ricker et al. 2015) and Gaia (Gaia Collaboration et al. 2018). The TESS lightcurve shows two distinct signals, which we extract and analyze in Section 3. A long-period sinusoid repeats every 12.0 hours, and is probably stellar rotation. A short-period dip superposed on an asymmetric sinusoid repeats every 10.7 hours. Analyzing the Gaia data in Section 4, we show that relative to its kinematic group, PTFO 8-8695 is a photometric binary, and suggest it also an astrometric binary. We discuss the puzzle pieces in Section 5. The orbital phase of the dip seems to have instantaneously changed over the past decade. In addition, other young stars show lightcurve morphologies similar to the short-period signal. We therefore argue that PTFO 8-8695 is a binary M dwarf in which one star shows a rotation signal, and the other shows transient dipping potentially caused by eclipses of plasma at the Keplerian co-rotation radius. Section 6 summarizes our main points.

2. THE DATA

2.1. TESS Observations

PTFO 8-8695 was observed by TESS with Camera 1, CCD 1, from December 15, 2018 to January 6, 2019, during the sixth sector of science operations (Ricker et al. 2015). The star was designated TIC 264461976 in the TESS Input Catalog (Stassun et al. 2018, 2019). The pixel data for an 11×11 array surrounding PTFO 8-8695 were averaged into 2-minute stacks by the onboard computer. Each 2048×2048 image from the CCD was also averaged into 30-minute stacks, and saved as a “full frame image” (FFI).

The 2-minute stacks for PTFO 8-8695 were reduced to lightcurves by the Science Processing Operations Center (SPOC) at NASA Ames (Jenkins et al. 2016). Our main analysis used the resulting Presearch Data Conditioning (PDC) lightcurve. The PDC lightcurve aperture used pixels chosen

to maximize the SNR of the total flux of the target (Smith et al. 2017a). Non-astrophysical variability was removed by fitting out trends common to many stars (Smith et al. 2017b).

As an independent check on the shorter cadence SPOC light-curve, we separately processed the 30-minute image stacks as part of the Cluster Difference Imaging Photometric Survey (CDIPS; Bouma et al. 2019). Our CDIPS lightcurve of choice used a circular aperture with radius 1 pixel.

To clean the data, we removed all points with non-zero quality flags (*e.g.*, Tenenbaum & Jenkins 2018). We also masked out the first and last 6 hours of each orbit, since there is often systematic red noise during those times. Both the CDIPS and PDC lightcurves showed a clear discontinuous “jump” in the last few days of orbit 20, which seemed likely to be an instrumental systematic. We correspondingly masked out times from BJD 2458488.3 until the end of the orbit. The PDC lightcurve initially had 15,678 points. The quality-flag cut removed 854 points; masking the orbit edges removed an additional 716; removing the final few days of orbit 20 removed an additional 1079. After cleaning, 83% of the initial flux measurements remained.

We normalized these points by dividing out the median flux. We opted to then subtract by unity to simplify subsequent interpretation. Many of these and subsequent processing steps were performed using *astrobases* (Bhatti et al. 2018).

2.2. Gaia Observations

2.2.1. Astrometry of PTFO 8-8695

Between July 25, 2014 and May 23, 2016, Gaia measured about 300 billion centroid positions of 1.6 billion stars (Gaia Collaboration et al. 2016; Lindegren et al. 2018; Gaia Collaboration et al. 2018). In the Gaia second data release (DR2), these CCD observations were used to estimate positions, proper motions, and parallax for the brightest 1.3 billion stars, including PTFO 8-8695 (Lindegren et al. 2018). There were 121 “good” observations of PTFO 8-8695, that is observations that were not strongly down-weighted in its astrometric solution. PTFO 8-8695 was assigned a Gaia DR2 identifier of 3222255959210123904. Its photometric brightness was measured using selected bands (G , R_p , and B_p) of the Gaia Radial Velocity Spectrometer (Cropper et al. 2018; Evans et al. 2018). We accessed the pipeline parameters for PTFO 8-8695 using the Gaia archive¹.

The majority of Gaia’s derived parameters for PTFO 8-8695 agreed with expectations from former studies (Briceño et al. 2005; van Eyken et al. 2012). One novelty however was that Gaia DR2 detected a 10.3σ “astrometric excess”. We comment on the significance and interpretation of this excess in Section 4.

2.2.2. Hierarchical Cluster Membership

Gaia also provided astrometric parameters for tens of thousands of young stars in the Orion complex. Stellar popula-

¹ gea.esac.esa.int/archive/

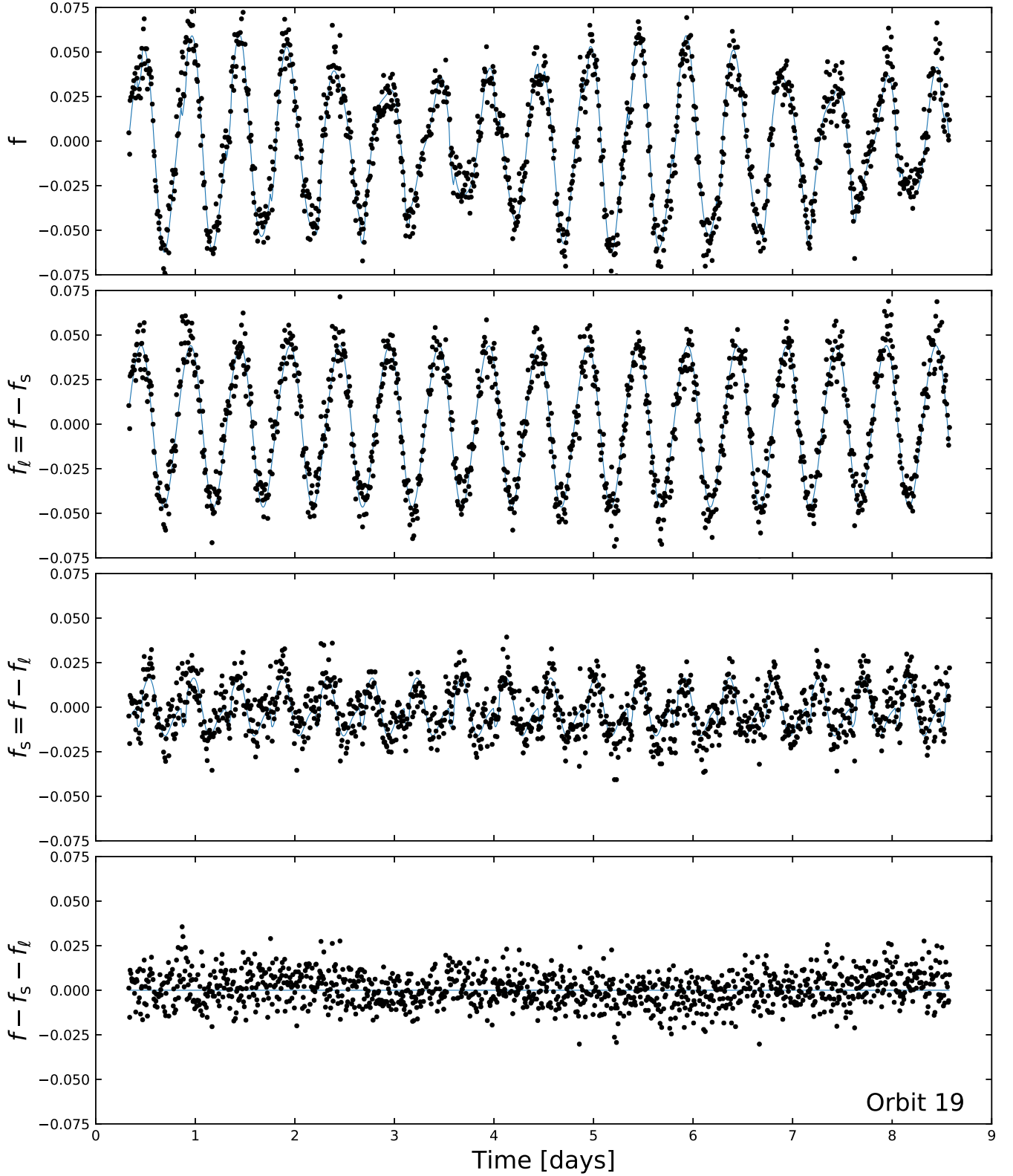


Figure 1. TESS lightcurve of PTFO 8-8695 (Sector 6, Orbit 19). *Top*: “Raw” PDCSAP mean-subtracted relative flux versus time. The beat period of 4.48 days is visible by eye. The preferred model plotted underneath the data includes 2 harmonics at the long period P_ℓ , plus 2 harmonics and a transit at the short period P_s . *Upper middle*: Long-period signal, equal to the raw signal minus the short-period signal. *Lower middle*: Short-period signal, equal to the raw signal minus the long-period signal. *Bottom*: residual. The data are binned from 2 to 10 minute cadence as a convenience for plotting and fitting.

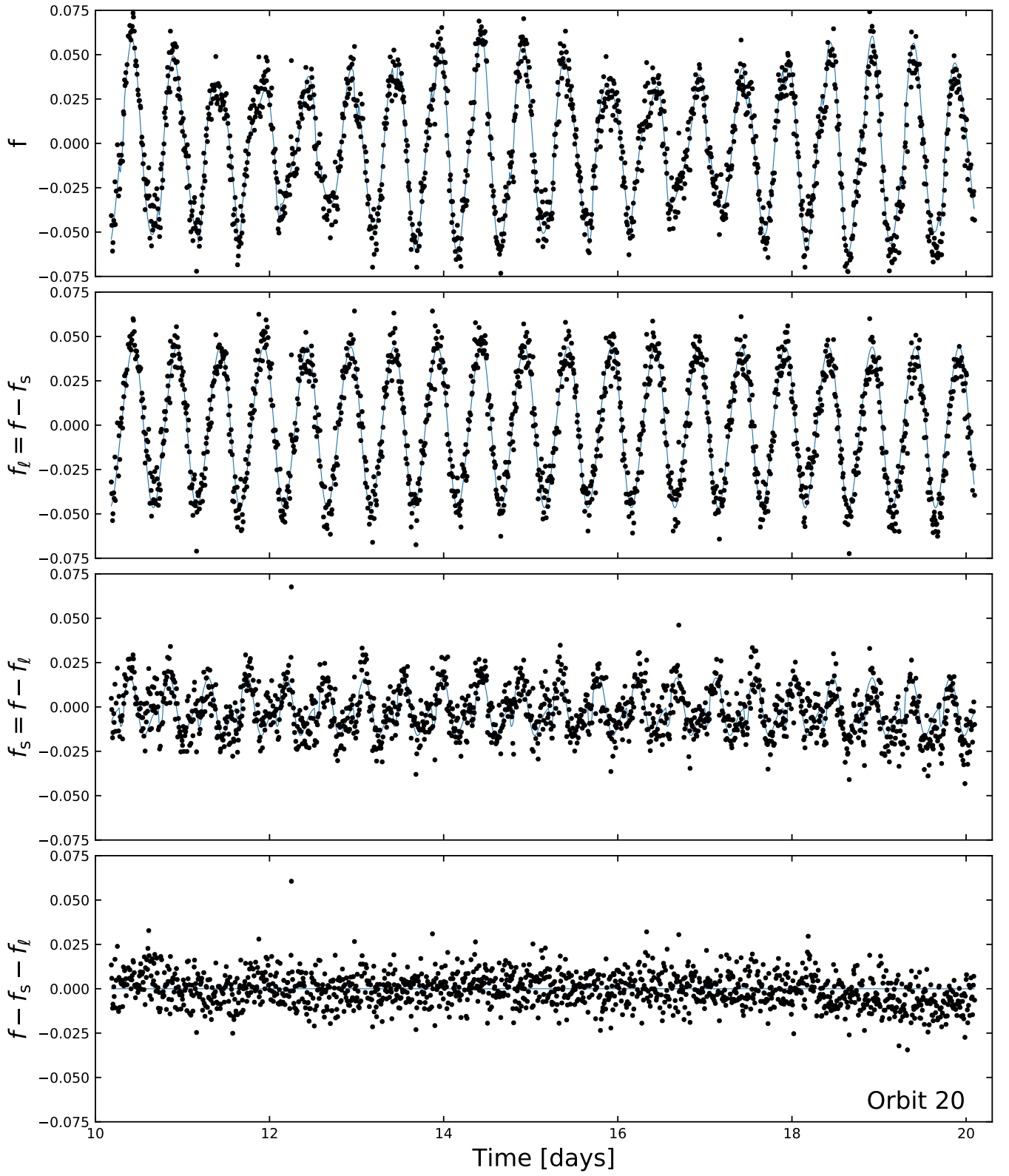


Figure 2. TESS lightcurve of PTFO8-8695 (Sector 6, Orbit 20). Panels are as in Figure 1.

tions in giant molecular cloud complexes are not monolithic; substructured groups are the norm (Briceño et al. 2007b). The Orion molecular cloud complex in particular has numerous subgroups, with ages spanning 0.5 to 15 Myr. For an incomplete sampling, see for instance Briceño et al. (2005); Jeffries et al. (2006); Briceño et al. (2007a); Kounkel et al. (2018) and Briceño et al. (2019).

PTFO 8-8695 was initially identified as a member of the Orion OB1a sub-association by Briceño et al. (2005) through combined photometry and spectroscopy. Later work by Briceño et al. (2007a) clarified that PTFO 8-8695 was in a kinematically distinct subgroup of Orion OB1a, named the “25 Ori” group after its brightest member. The 25 Ori group had an isochrone age of 7–10 Myr, and had a smaller disk fraction than younger nearby sub-associations (Hernández et al. 2007a).

With the Gaia astrometry, it has become clear that 25 Ori itself has further subgroups (Kounkel et al. 2018; Briceño et al. 2019). In describing the cluster membership of PTFO 8-8695, we follow the notation and results of Kounkel et al. (2018). These authors combined astrometric data from Gaia DR2 with near-infrared spectra from APOGEE-2 (Gunn et al. 2006; Majewski et al. 2017; Blanton et al. 2017; Zasowski et al. 2017; Cottle et al. 2018). They performed a hierarchical clustering on the six dimensional position and velocity information to identify subgroups within the Orion complex. From smallest to largest, PTFO 8-8695 was identified as a member of the following hierarchical subgroups:

$$25 \text{ Ori-1} \subset 25 \text{ Ori} \subset \text{Orion OB1a} \subset \text{Orion D}, \quad (1)$$

where from set-notation, ‘ \subset ’ denotes “is a proper subset of”. 25 Ori-1 is the largest subgroup of 25 Ori, with 149 identified members. Its mean age from its CMD was found to be 6.9 Myr, and from its HR diagram 8.5 Myr (Kounkel et al. 2018). Kounkel et al. (2018) identified seven other smaller groups in the Orion complex near the Be star 25 Ori. These groups received higher numbers, *e.g.*, 25 Ori-2 (Age_{CMD} = 15.1 Myr; Age_{CMD} = 12.9 Myr; see also Briceño et al. 2019).

These details concerning the group membership for one object may seem cumbersome to those accustomed to comparing “young cluster members” with “old field stars”. Though all members of the Orion complex are indeed young relative to the field, these details are essential for assessing any evidence for photometric binarity in PTFO 8-8695, because of the degeneracy between stellar luminosity and age for pre-main-sequence stars. Having a clean sample of tightly spatially and kinematically associated reference stars minimizes contamination not just from the field, but from older and younger members of the Orion complex itself.

3. TESS ANALYSIS

3.1. Inspection

Our initial inspection of the TESS lightcurve, in both its 2-minute PDCSAP and 30-minute FFI forms, showed a strong sinusoidal beat signal (Figures 1 and 2, top panel).

As a precursor to more detailed analysis, we calculated generalized Lomb-Scargle periodograms using *astrobases*

(Lomb 1976; Scargle 1982; VanderPlas & Ivezić 2015; Bhattacharya et al. 2018). The two largest peaks in the Lomb-Scargle periodogram of the lightcurve were separated at a “short” period $P_s \approx 0.448$ days and a “long” period $P_\ell \approx 0.499$ days. The P_ℓ peak had the greater power of the two. Smaller harmonics surrounding each of these two dominants peaks were also present.

The peak-to-peak lightcurve amplitude at maximum, when the two signals constructively interfere, is about 14%. At minimum, the peak-to-peak amplitude is about 6%. Assuming the signals are just two sinusoids, algebra tells us that the peak-to-peak amplitudes should therefore be 10% for the long-period signal, and 4% for the short-period signal. These order-of-magnitude numbers will turn out to be roughly correct.

Initial signal-processing experiments fitting out splines or sinusoids showed that after subtracting out the long-period signal, the short-period signal dominated the periodogram, and vice-versa. However it quickly became clear that it would be beneficial to simultaneously model each signal, in order to preserve the power at each frequency.

3.2. Lightcurve Model

We fitted the lightcurve as a linear combination of Fourier harmonics at the short and long periods, plus a transit at the short period. Symbolically, the total flux f is given as

$$f = f_s + f_\ell = f_{\text{transit},s} + f_{\text{Fourier},s} + f_{\text{Fourier},\ell}, \quad (2)$$

where f_s is the flux at the short period, and f_ℓ is the flux at the long period. Writing out the Fourier terms,

$$f = f_{\text{transit},s} + \sum_{n=1}^N A_n \sin(n\omega_s t) + \sum_{n=1}^N B_n \cos(n\omega_s t) + \sum_{m=1}^M A_m \sin(m[\omega_\ell t + \phi_\ell]) + \sum_{m=1}^M B_m \cos(m[\omega_\ell t + \phi_\ell]), \quad (3)$$

for N and M the total number of harmonics at the short and long periods, respectively, A_i and B_i the amplitudes for each harmonic term (potentially negative), and $\omega_i = 2\pi/P_i$ the angular frequency for i the short or long period index. We fixed the “phase-offset” for the short period signal to be zero, and let the reference time for the long period signal float by introducing ϕ_ℓ . Since we did not a priori know how many harmonics would be appropriate, we considered a number of different choices for N and M , and used the Bayesian information criterion to choose the appropriate model (Table 1).

As an example, one possible model could be a transit, plus $N = 2$ harmonics of sines and cosines at the short period, plus $M = 1$ harmonics at the long period. For this case the free parameters would be as follows. For the transit, we would fit for the impact parameter, the planet-to-star radius ratio, two quadratic limb darkening parameters, the planet orbital period (equal to the short period), the reference time for the transit, and the mean flux. There would be $2N = 4$ additional Fourier amplitudes at the short period, plus $2M = 2$ Fourier

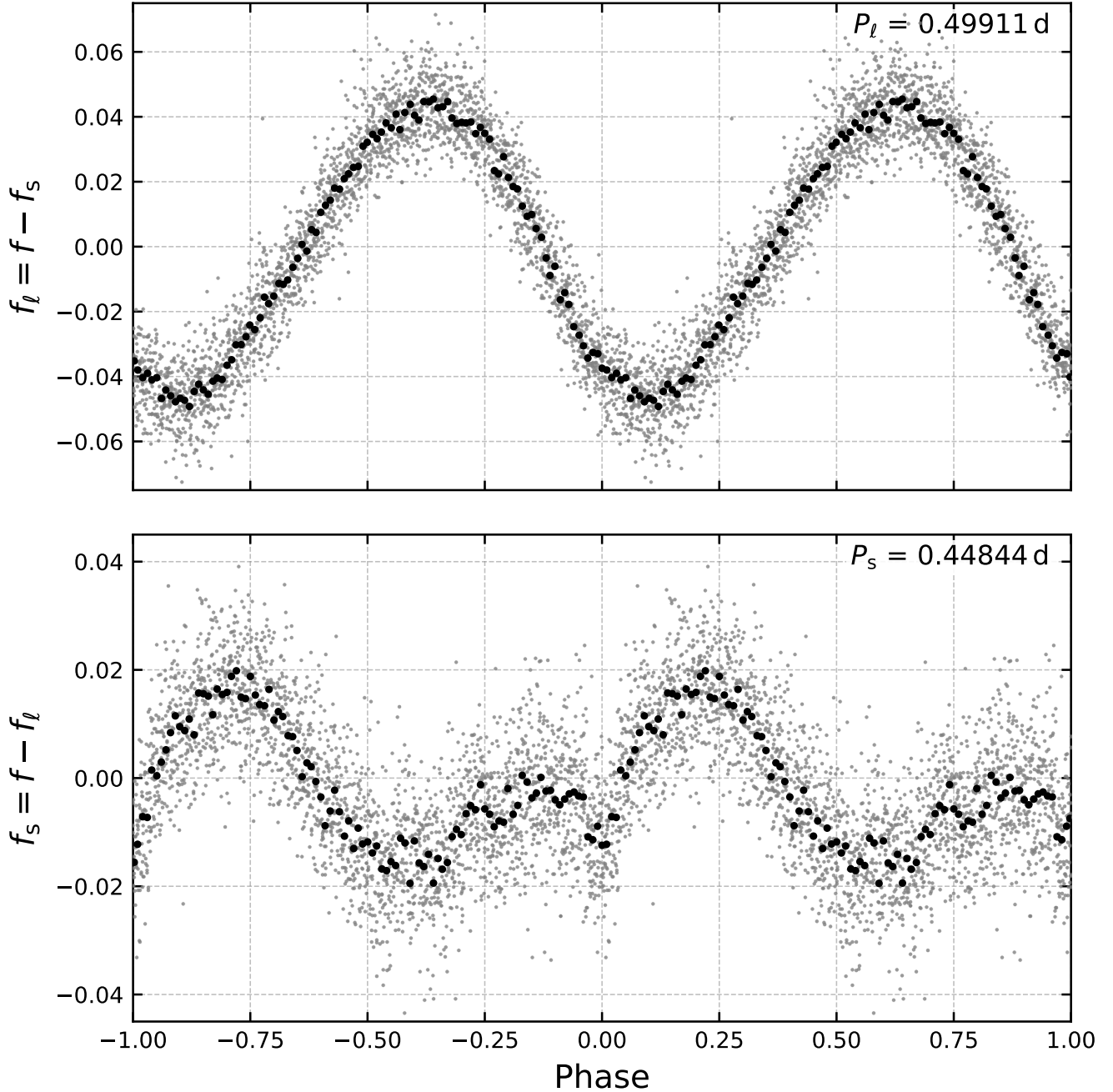


Figure 3. Phase-folded long and short-period signals. *Top:* Long-period signal, as in Figure 1. *Bottom:* Short-period signal. The reference phase is set to the “planetary” dip. Gray points are the 10 minute cadence PDCSAP flux. Black points are binned to 100 points per period.

amplitudes at the long period, and well as the long period itself and its phase. For this case, we therefore fitted 14 free parameters.

We implemented and fitted the models using `PyMC3`, which is built on `theano` (Salvatier et al. 2016; Theano Development Team 2016). For the Fourier terms, we used the default math operators. For the exoplanet transit, we used the model and derivatives implemented in `exoplanet` (Foreman-Mackey et al. 2020). Our priors are listed in Table 2. To speed up the fitting, we re-sampled the cleaned 2

minute lightcurves to 10 minute binning. We correspondingly scaled the uncertainties in the flux measurements by a factor of $\sqrt{5}$. Before sampling, we initialized each model to the maximum a posteriori (MAP) solution. We then sampled using `PyMC3`’s gradient-based No-U-Turn Sampler (Hoffman & Gelman 2014), and used \hat{R} as our convergence diagnostic (Gelman & Rubin 1992). We tested our ability to successfully recover injected parameters using synthetic data before fitting the PTFO 8-8695 lightcurves.

3.3. Fitting Results

We considered nine models, with the number of harmonics per frequency N and M ranging from one to three. To select our preferred model, we used the Bayesian information criterion (Table 1). The model with the lowest BIC had two harmonics at the short 10.74 hr period, and two harmonics at the long 11.96 hr period. The next-best model had an additional harmonic at the longer period ($M = 3$), but was otherwise identical. All nine models have reduced χ^2 ranging between 1.37 and 1.51, which suggests a plausible though imperfect agreement between the data and fitting results. The best-fit parameters for the lowest BIC model are given in Table 2.

To explore where each model succeeded and failed, we split the raw signal into its respective components (Figures 1 and 2). We also examined the phase-folded signals (Figure 3).

In every model, the 11.96 hr variability is a simple sinusoid with peak-to-peak amplitude $\approx 10\%$. The 10.74 hr variability is always more complex. A dip of depth $\approx 1.2\%$, fit in our model as a transit, lasts ≈ 0.75 hours. Superposed on the dip is an asymmetric sinusoid with peak-to-peak amplitude of about 4%. The asymmetric sinusoid peaks near phase 0.25, and reaches minimum brightness between phases -0.5 and -0.25. The flux at phase ≈ -0.33 shows what could be a discontinuous jump, shortly after reaching minimum (Figure 3). This jump was visible in each of the nine models we considered.

The periodogram of the final residual (Figures 1 and 2 bottom row) shows a weakly significant, poorly resolved peak at ≈ 8 days, consistent with the visual impression in the time domain that there could be a weak long-period signal present.

4. BINARITY ANALYSIS

4.1. Visual Binarity

The TESS pixels are $\approx 21''$ per side. Before making any interpretations, we needed to consider whether light from known neighboring stars could have affected the photometry. The scene is shown in Figure 4. In the upper panels, the pixels used to measure the background level in the SPOC lightcurve are indicated with an ‘x’ hatch, and the pixels used in the final lightcurve aperture are shown with the ‘/’ hatch.

The target star, PTFO 8-8695 (TIC 264461976), has a T -band magnitude of 14.0, and its position is shown with a star. The other (unlabeled) star inside the target aperture, TIC 264461979, has $T = 16.8$ and so cannot contribute a signal with relative amplitude 10%. The only neighbor that is sufficiently close and bright that its light might contaminate the target star is TIC 264461980, with $T = 14.8$, which we dub “Star A”. Star A is $23.6''$ NW of our target, and based on the magnitude difference could contribute up to 48% the flux of our target star, PTFO 8-8695.

Because PTFO 8-8695 was previously identified to have periodicity consistent with our measurement of P_s , our main concern regarding blending was the degree to which we could be certain that the long-period signal at P_ℓ also originated

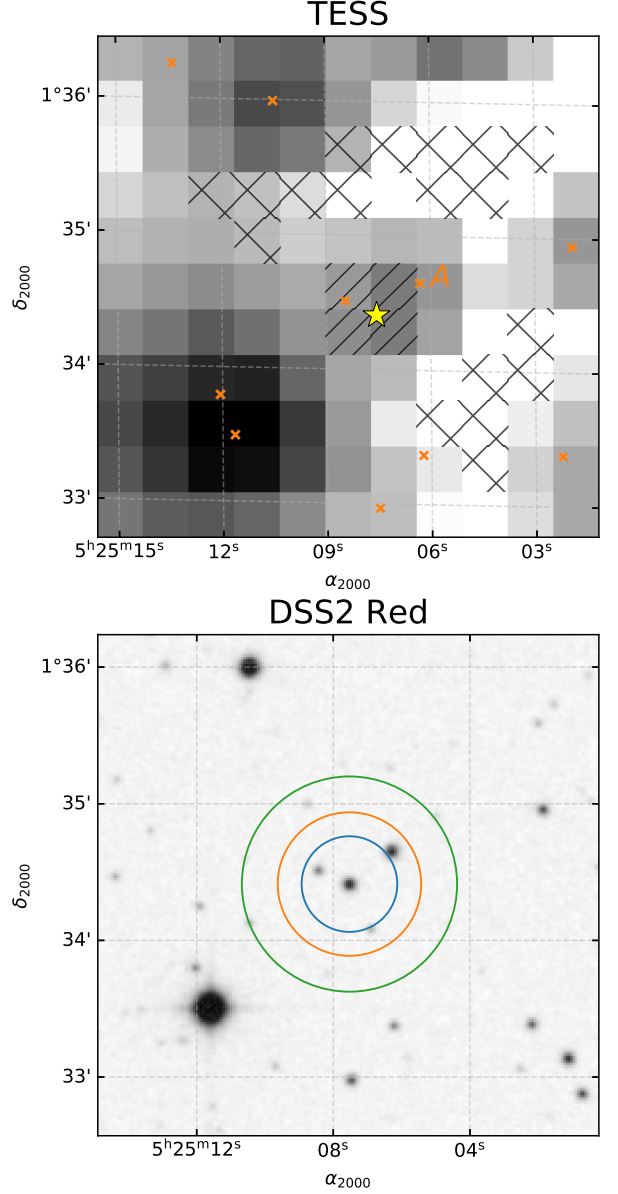


Figure 4. Scene used for blend analysis. *Top:* Mean TESS image of PTFO 8-8695 over Sector 6, with a log-stretch. The position of PTFO 8-8695 is shown with a yellow star. Neighbors with $T < 17$ are shown with orange crosses. The apertures used to measure the background and target star flux are shown with x and / hatches, respectively. *Bottom:* Digitized Sky Survey R -band image of the same field, with a linear stretch. The circles show apertures of radii 1, 1.5, and 2.25 pixels used in part of our blend analysis. The pixel level TESS data show that “Star A” does not contribute variability at either of the two observed periods (see Section 4.1).

from PTFO 8-8695. We took two approaches to verifying the source of the long-period signal.

First, we examined the CDIPS FFI lightcurves of the target, which were available on MAST (Bouma et al. 2019). The maximal peak-to-peak beat amplitude was constant across apertures of radii 1, 1.5, and 2.25 pixels to visual pre-

cision ($\lesssim 1\%$). If Star A were the source of the long-period variability, we would expect the peak variability amplitude to be smallest in the 1 pixel aperture, based on the separation of the sources (Figure 4, bottom). From this test alone, it seems unlikely that Star A is the source of the long-period signal.

Second, we examined the 2-minute lightcurve of each pixel in the scene individually. We opted to use the interactive tools implemented in `lightcurve` (Lightcurve Collaboration et al. 2018). If Star A were the source of the long-period variability, we would expect the pixels nearest to Star A to show a sinusoidal signal with amplitude exceeding 10%. The data do not support this possibility. The pixel directly below Star A does not clearly show the sinusoidal variability, and the peak-to-peak variability in that pixel is $\lesssim 8\%$. In contrast, the south-easternmost pixel within PTFO8-8695’s aperture (the pixel furthest from Star A that was used in the optimal aperture) shows the P_ℓ sinusoidal variability signal at $\approx 14\%$ amplitude. We conclude that within the resolution of the Gaia DR2 source catalog, the P_s and P_ℓ signals originate from PTFO8-8695. From Ziegler et al. (2018), we can surmise that stellar companions wider than $\approx 1''$ (349 AU) and within $\Delta G \approx 3$ magnitudes of PTFO8-8695 would have likely been detected through this approach.

van Eyken et al. (2012) obtained stronger constraints on possible stellar companions using the NIRC2 camera on Keck II. They reported 3σ H -band magnitude difference limits of 4.3, 6.4, and 8.9 at angular separations of 0.25, 0.5, and 1.0 arcseconds (87, 175, and 349 AU). They also detected a point-source, not present in Gaia DR2, 7.0 magnitudes fainter than the target, and $1.8''$ north-east. Due to the brightness difference, this coincident star² cannot be the source of our signals.

While long-baseline radial velocity measurements could provide complimentary lower limits on companion masses and separations, the RV data for PTFO8-8695 are rather poor owing to the stellar faintness. The longest single-instrument baseline in the literature appears to be 5 Keck/HIRES measurements acquired over 10 days in April 2011 by van Eyken et al. (2012). The RV RMS over that 10 day span was 1.6 km s^{-1} , consistent with the measurement precision. Though Yu et al. (2015) acquired 22 further Keck/HIRES observations over one night in December 2013, these points seem to not have been reduced to velocities. Further Keck/HIRES measurements of this target could confirm or refute the existence of possible binary companions.

4.2. Photometric Binarity

Aside from visual binarity, we can also check the Gaia data for photometric binarity. To assemble a set of stars coeval with PTFO8-8695, we used the 25 Ori-1 members identified by Kounkel et al. (2018), and discussed in Section 2.2.2.

² This companion was claimed to be a potential planetary-mass object (Schmidt et al. 2016). Subsequent analysis of its colors showed that it is a background star (Lee & Chiang 2018).

To define a set of non-member stars that nonetheless had comparable selection functions, we defined a reference “neighborhood” as the group of at most 10^4 randomly selected non-member stars within 5 standard deviations of the mean 25 Ori-1 right ascension, declination, and parallax. We queried Gaia DR2 for these stars using `astroquery` (Ginsburg et al. 2018). This yielded 1,819 neighbors. While some of these stars may indeed be members of the Orion complex, or even of 25 Ori-1, enforcing this cut on positions and parallaxes ensures that we are querying stars with comparable amounts of interstellar reddening.

We examined the resulting five-dimensional right ascension, declination, proper motions, and parallaxes. The first point we noted was that 25 Ori-1 was a clearly defined overdensity in each dimension—the cluster exists, and is distinct from the neighborhood. PTFO8-8695 was also within the cluster in each of these projected dimensions.

Given our detection of two separate signals, whether PTFO8-8695 could be a photometric binary was of great interest. Figure 5 shows the HR diagram we constructed to assess this issue. The diagram shows that PTFO8-8695 is ≈ 0.75 magnitudes brighter than the average 25 Ori-1 star of the same color. In other words, it is about twice as bright. It also seems to be coincident with the photometric binary track of the cluster, which has a few other stars.

The implication is that either (i) PTFO8-8695 is notably younger than the kinematically identical 25 Ori-1 members, or (ii) PTFO8-8695 is a photometric binary. Since there is no a priori reason to suspect an age difference, but we have resolved two separate photometric signals, the binary interpretation seems somewhat more likely.

4.3. Astrometric Binarity

A separate possible line of evidence for binarity is the Gaia DR2 astrometry. As noted in Section 2, the Gaia DR2 solution for PTFO8-8695 shows a 10.3σ astrometric excess. This astrometric excess indicates the degree to which a single-source model fails to explain the observed astrometric measurements. Specifically, the single-source astrometric model yielded $\chi^2 = 325.2$. There are 121 astrometric measurements, and 5 free parameters, and therefore 116 degrees of freedom. The reduced χ^2 is 2.80. The majority of stars with comparable brightness in Gaia do not show such poor goodness-of-fit (see Lindegren et al. 2018, Appendix A).

Potential explanations for the poor astrometric fit include photometric variability and unresolved stellar binarity (e.g., Rizzuto et al. 2018; Belokurov et al. 2020). If photometric variability were the cause, we would expect comparably faint stars in the same kinematic group of Orion to show similar astrometric excesses, as the majority of young stars are highly variable.

Using the same 149 members in the 25 Ori-1 subgroup, we calculated the astrometric reduced χ^2 for each member. We then queried the CDIPS lightcurve database at MAST (Bouma et al. 2019) to find the subset of members that were at least as variable as PTFO8-8695. We measured the variability amplitude by taking the difference of the 95th and 5th

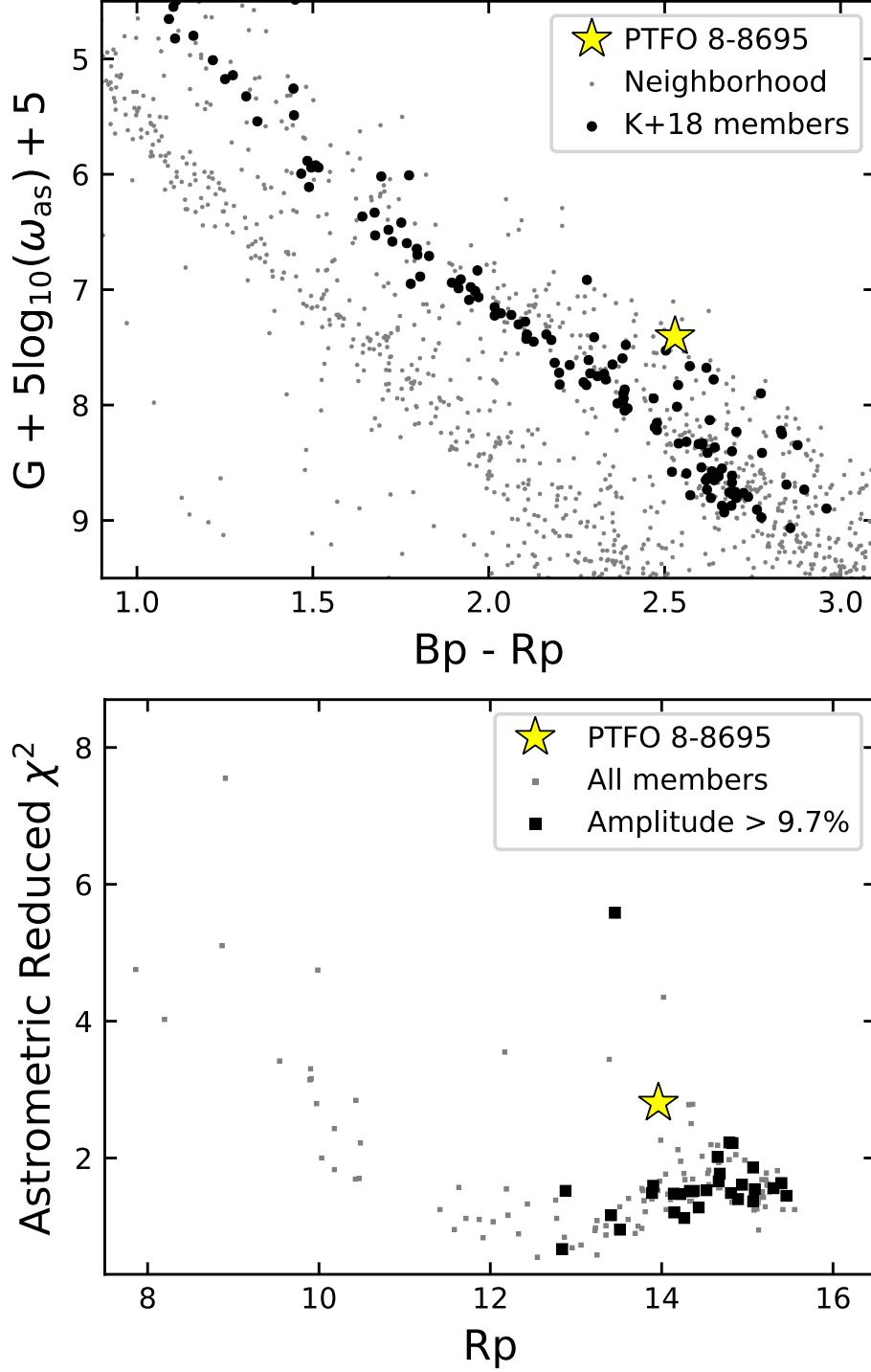


Figure 5. Evidence for binarity in PTFO 8-8695. *Top:* Hertzsprung-Russell diagram of PTFO 8-8695 and late-type members of 25 Ori-1. Members of the 25 Ori-1 group (black circles) were identified by Kounkel et al. (2018). The “neighborhood” (gray circles) is non-member stars within 5 standard deviations of the mean 25 Ori-1 right ascension, declination, and parallax. It contains members of the Orion complex with its full spread of ages, in addition to field interlopers. G denotes Gaia broadband magnitudes, Bp Gaia blue, Rp Gaia red, and ω_{as} the parallax in arcseconds. The x -axis limits are set to show only K and M dwarfs, to accentuate PTFO 8-8695’s separation from the single-star sequence. *Bottom:* Astrometric goodness-of-fit versus Rp magnitude for 25 Ori-1 members. The single-source astrometric model for PTFO 8-8695 provides a poor fit, which could be due to stellar variability or binarity. Cluster members that are at least as variable as PTFO 8-8695 show lower astrometric excesses (black squares), suggesting binarity as the probable root cause.

percentiles of the flux. This yielded 30 stars of equal or greater variability. The lower panel of Figure 5 shows the reduced χ^2 as a function of stellar brightness. PTFO8-8695 is in the upper 90th percentile of stars showing astrometric excesses within the 25 Ori-1 group. Relative to other M-dwarf group members with comparable brightnesses and variability characteristics, PTFO8-8695 still stands out as behaving astrometrically poorly. Ultimately, we will have to wait for the full release of the nominal Gaia mission to definitively determine whether the astrometric excess is caused by stellar binarity or photometric variability. Nonetheless the fact that comparably variable stars do not show comparably large astrometric excesses suggests that stellar binarity is indeed the root cause.

5. DISCUSSION

5.1. Long Period Sinusoid

The standard interpretation for 11.96-hour sinusoidal modulations of a pre-main-sequence M dwarf is stellar rotation. This is the dominant signal in the system with 10% amplitude, and there is no evidence to suggest that this signal has any other origin.

The discovery study by [van Eyken et al. \(2012\)](#) saw an alias of the same signal (*e.g.*, their Figure 7), and identified it as a periodogram peak at 0.9985 ± 0.0061 days. They ascribed it to their observing cadence, because of its close correspondence to the sidereal day. While the TESS data can show significant reflected light from the Earth (*e.g.*, [Luger et al. 2019](#)), our pixel-level analysis showed that the signal is specific to only pixels near PTFO8-8695, and no other pixels. We therefore conclude that the signal is not a systematic.

We are not the first to reach the conclusion that the long period sinusoidal modulation is astrophysical. A study by [Koen \(2015\)](#) identified the same modes and aliases as [van Eyken et al. \(2012\)](#), but argued that the signal was astrophysical (however they were still unsure of the exact period). Using photometry from the YETI global telescope network, [Raetz et al. \(2016\)](#) eventually came to the conclusion that the 0.50d signal was indeed from stellar rotation. The TESS data strongly support this conclusion.

5.2. Short Period Dip

The TESS lightcurve shows a dip that lasts about 45 minutes, and seems to re-occur every 10.74 hours (Figures 1, 2, 3). The dip duration is roughly the same as that observed by previous investigators ([van Eyken et al. 2012](#); [Yu et al. 2015](#)). The 1.2% depth is similar to what has been observed in the near-infrared ([Onitsuka et al. 2017](#)). However the dip depth seems likely to have evolved over time between being not present at all, to a maximum of $\approx 5\%$ ([Koen 2015](#); [Yu et al. 2015](#); [Tanimoto et al. 2020](#), *e.g.*).

One particularly interesting feature of the dip is its epoch. Over the past decade, many investigators have observed PTFO8-8695. Its dips do not always occur on a perfectly linear ephemeris ([Yu et al. 2015](#)). In fact, [Tanimoto et al. \(2020\)](#) recently provided stark evidence for different behavior altogether: over a time-span of years, the dip “splits” into distinct

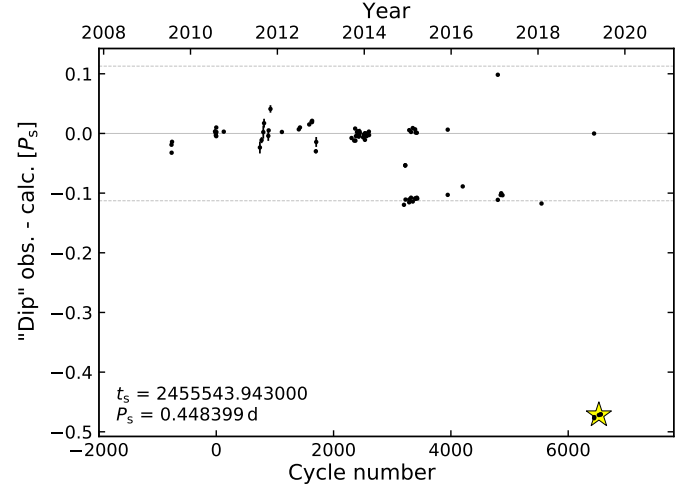


Figure 6. Timing residuals for PTFO8-8695b from a decade of monitoring. Black points are times of dips, minus the indicated linear ephemeris. The y-axis is given in units of phase for the short-period signal. The star shows the binned TESS ephemeris. Dips have been observed by [van Eyken et al. \(2012\)](#), [Ciardi et al. \(2015\)](#), [Yu et al. \(2015\)](#), [Raetz et al. \(2016\)](#), [Onitsuka et al. \(2017\)](#), and [Tanimoto et al. \(2020\)](#). Certain dips (*e.g.*, the one at phase 0 in mid-2019) are consistent with noise, and were likely reported because dips were expected, rather than convincingly observed. Horizontal dashed lines are drawn at $\pm(P_\ell - P_s)/P_s$, highlighting either a numerical coincidence or an observational bias. The orbital phase observed by TESS (lower-right) is consistent with that of [Tanimoto et al. \(2020\)](#).

groups at particular repeating phases. See for instance their Figures 2 through 4. Fitting a decade of observations, they provided the following linear ephemeris, which we did not find any need to update.

$$t_0 \text{ BJD}_{\text{TDB}} = 2455543.943 \pm 0.002 \quad (4)$$

$$P = 0.4483993 \pm 0.0000006 \text{ d}. \quad (5)$$

In Figure 6, we show the phase of the dip we detect in the TESS data, relative to their ephemeris. It agrees with the independent December 2018 measurements by [Tanimoto et al. \(2020\)](#): the dip has drastically shifted phase over the past decade.

Figure 6 shows two additional strange features: (i) multiple dips per cycle, and (ii) a set of dips numerically coincident with phase $(P_\ell - P_s)/P_s$. The observation of multiple dips per cycle in 2015 was seen independently by both [Yu et al. \(2015\)](#) and [Tanimoto et al. \(2020\)](#). It therefore seems credible. Inspecting the [Tanimoto et al. \(2020\)](#) lightcurves, the claim of multiple dips per cycle in December 2018 at phase 0 and -0.47 seems less plausible—the phase -0.47 dips are strongly detected, while the suggested phase 0 dip is not clearly present in the data.

We are not sure what to make of the numerical coincidence. The ratio of long to short periods is roughly 10:9. It is not clear that this would obviously translate into an ob-

servational bias unless by some fluke three season’s worth of observations managed to only observe every ninth dip. This is of course not the case, and we therefore leave this curiosity as observation *sans* interpretation.

5.3. Short Period Out-of-Dip Modulation

Visually, the out-of-dip modulation at the 10.74 hour period resembles a slightly asymmetric sinusoid (Figure 3). Non-zero contributions in both the first and second harmonics are detected (Table 2). The first sine and cosine harmonic both have amplitudes of roughly $0.9 \pm 0.1\%$. The second sine harmonic has amplitude $0.16 \pm 0.07\%$, so is non-zero at a significance of only 2.3σ . The second cosine harmonic has negative amplitude $0.53 \pm 0.06\%$. In our sign convention, the fact that it is negative means that this component peaks at phase 0.25 and 0.75.

5.3.1. Ellipsoidal Variability?

If there were a giant planet transiting PTFO8-8695, it would tidally distort the host star, and cause ellipsoidal photometric modulations that also peak at quadrature (see Shporer 2017). Interpreting the second cosine harmonic as planet-induced tidal distortion, it would imply a minimum planet mass $M_p \sin i$ of $3.8 M_{\text{Jup}}$. For this estimate, we assumed $R_* = 1.39 R_\odot$, and $M_* = 0.39 M_\odot$ (van Eyken et al. 2012). This ellipsoidal amplitude is larger than the typical modulations induced by close-in giant planets because the host star is puffy, and still on the pre-main-sequence.

The planetary interpretation however does not readily explain the first sine and cosine harmonics. Interpreting the sine component as Doppler beaming would imply a secondary mass greater than the primary ($0.86 M_\odot$). Interpreting the cosine component as reflected or emitted light from the planet’s surface is nonsensical because the sign is wrong—the planet would need to be *absorbing* light.

5.3.2. Similar Lightcurves

When physical explanations are not forthcoming, taxonomy can be a useful exercise. To our knowledge, of order 10-20 lightcurves with similar morphologies have been seen in surveys of low-mass weak-lined T Tauri stars in regions including ρ Oph, Upper Sco, Taurus, and perhaps the Pleiades (Rebull et al. 2016; David et al. 2017; Stauffer et al. 2017, 2018; Rebull et al. 2018, 2020). These surveys were performed using K2 (Howell et al. 2014). We downloaded a few of these lightcurves from MAST, opting for the EVEREST reductions (Luger et al. 2016, 2018). They are plotted in Figure 7.

These lightcurves have been phenomenologically classified as “persistent flux dips” or “transient flux dips”, based on whether their depths and durations show variability over the 90-day K2 campaigns (Stauffer et al. 2017). As Stauffer et al. (2017) explain, these objects are morphologically distinct from “scallop shell” lightcurves, and are present in stars at more advanced evolutionary disk stages than the “dipper” stars (Ansdell et al. 2016; Cody & Hillenbrand 2018). The

persistent and transient flux dip stars all show angular dips that are cannot be explained with starspots. They typically have the following properties.

1. Weak-lined T Tauri stars.
2. Spectral type typically M2-M5 (e.g., Rebull et al. 2018, Figure 20).
3. Ages $\lesssim 100$ Myr.
4. Stars typically lack spectroscopic accretion indicators
5. Phased lightcurves show shallow, angular dips, usually superposed on large-amplitude smooth variability. The latter is interpreted as stellar rotation.
6. Rotation is fast—usually between 0.5 and 2.0 days.
7. Rarely any infrared excess (never any W4 detection; only a few cases with W3 detections).
8. Can show multiple dips per cycle.
9. Dip depths, durations, and phases can vary over just a few cycles (e.g., EPIC 204143627).
10. Dip depths can change after flares.
11. Rare at a population level: $\lesssim 1\%$ of relevant stars (Rebull et al. 2018).

The 10.74 hour signal in PTFO8-8695 meets all of these criteria. This is the first connection of PTFO8-8695 with this class of objects because the TESS lightcurve was needed to resolve the different rotation signals.

There are two crucial additional points concerning the transient flux dips. First, the dip durations seem to scale linearly with their periods (Stauffer et al. 2017, Figure 26). In the usual idealized limits, the transit duration T of a point source across the stellar disk scales as $T \propto R_*(P/M_*)^{1/3}$ (Winn 2010). While the shortest period ≈ 0.5 -day transient flux dip stars have dip durations consistent with point sources, at longer periods of 1 to 5 days the dip durations become many hours, and far too long for a point-source origin.

Second, between 40-50% of the transient flux dip stars discovered in ρ Oph and Upper Sco show two Lomb-Scargle periods, and so are apparently binaries (Stauffer et al. 2017, Table 1). This is higher than the main-sequence companion fraction of $\text{CF}_{0.1-0.5 M_\odot}^{\text{MS}} = 33 \pm 5\%$ (Henry et al. 2006; Duchêne & Kraus 2013). Low-mass pre-main-sequence stars however have been shown to companion fractions up to twice as high in dispersed clusters such as Upper Sco and Taurus (Kraus et al. 2008, 2011). A detailed high-resolution imaging survey would be necessary to determine whether the transient flux dip stars truly have any distinct population-level binarity properties relative to other young low-mass stars.

5.4. Physical Interpretation

The evidence for binarity in PTFO8-8695 is as follows. First, the star is photometrically twice as bright as stars of the same color in its kinematic group (Figure 5). Second, it shows two distinct photometric signals. These points alone suggest binarity (Stauffer et al. 2018). For the case of PTFO8-8695, there is a third line of evidence: the Gaia

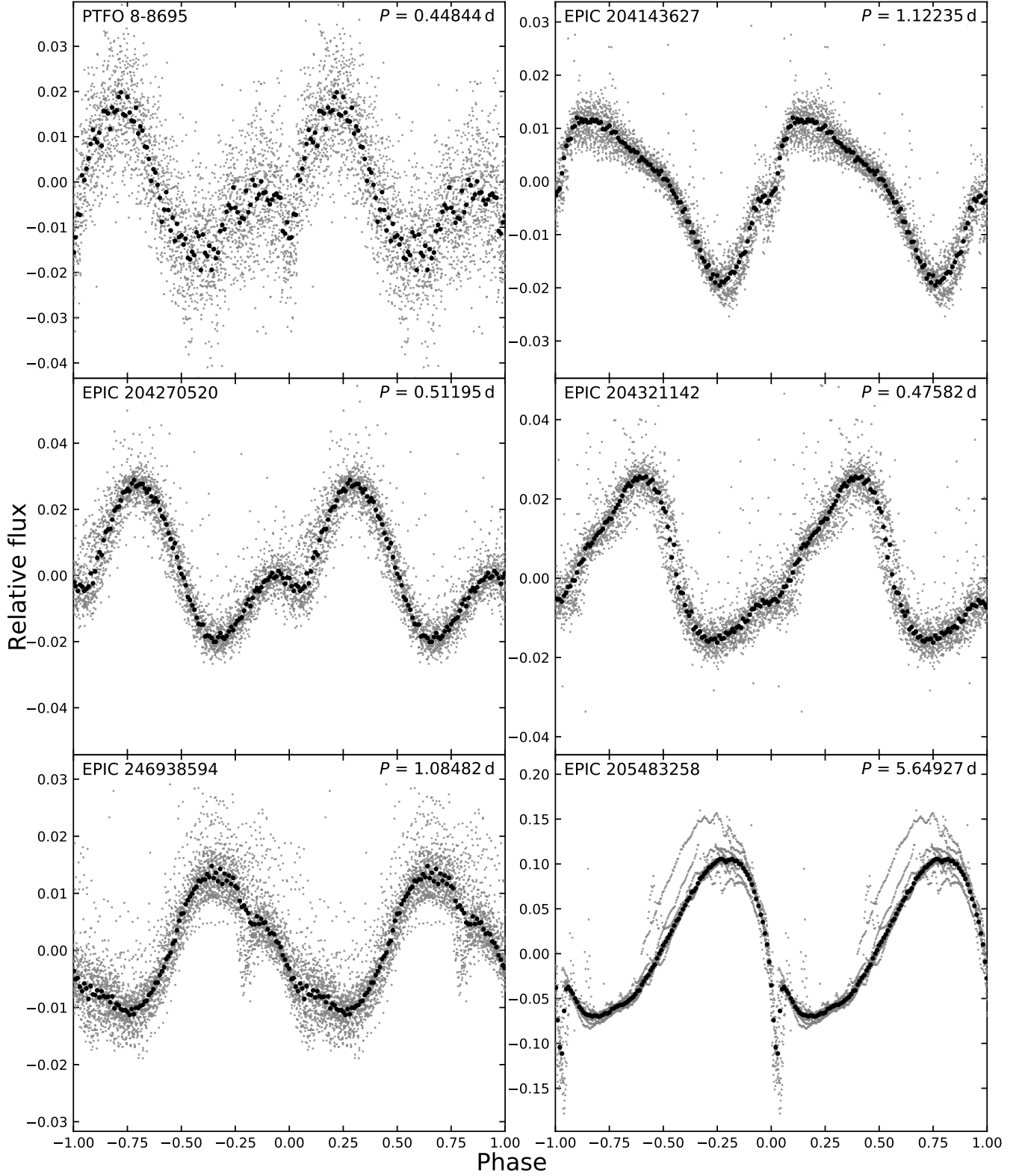


Figure 7. PTFO8-8695 and its brethren. Five transient and persistent flux dip stars selected based on their visual similarity to the short-period signal in PTFO8-8695 are as shown. They include EPIC 204143627, EPIC 204270520, EPIC 204321142, EPIC 246938594, and EPIC 205483258 (RIK-210). RIK-210 has the longest period of any of these objects. All the analogs displayed are either in Taurus or Upper Sco, and meet the characteristics of Section 5.3.2. We found these objects through studies by [Stauffer et al. \(2017\)](#), [David et al. \(2017\)](#), and [Rebull et al. \(2018\)](#).

astrometry shows a poor goodness-of-fit to a single-source model. While this could be caused by stellar variability, cluster members that are at least as variable still show PTFO 8-8695 to be an outlier. Therefore the astrometric excess is a suggestive third line of evidence for binarity in PTFO 8-8695. We take these three points combined to imply that PTFO 8-8695 is probably a binary.

Based on the lack of an infrared excess seen by Yu et al. (2015), the primordial gas disks seem to have been depleted³ around both stars in PTFO 8-8695. The stars are therefore no longer magnetically locked to their disks. This is consistent with the \approx half-day periodicities of both rotation signals: young disked M dwarfs typically rotate with periods of two days or more due to magnetic locking (e.g., Rebull et al. 2020). If the two stars are within ≈ 50 AU of each other, as required by the NIRC2 adaptive optics imaging, then it would also be expected that the stars would truncate the outer edges of their respective disks, in a manner seen at the population level in exoplanetary systems (Kraus et al. 2016; Moe & Kratter 2019). This hard outer boundary condition could propagate to the inner disk and affect its evolution.

The main physical question is what causes the transient dipping. This is an unsolved problem not only for PTFO 8-8695 but also for an emerging class of similar young rapidly rotating M-dwarfs. Many possible explanations have been detailed by Rebull et al. (2016), David et al. (2017), Stauffer et al. (2017), and Zhan et al. (2019). Their disfavored explanations include that the dips are caused by (i) eclipsing binaries; (ii) “dipper”-flavor Class-I or Class-II disks; (iii) eclipses of prominences; (iv) high-latitude accretion hotspots; (v) high-latitude starspots; or (vi) dust clouds of plausible composition. We also view the possibility of (vii) tidally disrupted planetary or cometary material to be implausible, given the synchronicity between dip and rotation periods seen across many systems.

The explanations that are not yet ruled out include (i) transiting clumps of gas at the Keplerian corotation radius; (ii) transits of enshrouded protoplanets; (iii) occultations of starspots by an optically thick disk. The first and last explanations offer added appeal because they are flexible enough to explain not only the transient and persistent-dip M-dwarfs, but also the “scallop shell” M-dwarfs (Stauffer et al. 2017). Despite this appeal, the possibility of distinct mechanisms explaining these distinct variability classes remains open.

The evolution of PTFO 8-8695 over the past decade (Figure 6) could offer important hints. Specifically, PTFO 8-8695’s transition between having none, one, and multiple dips per cycle seems important. It strains the “enshrouded protoplanet” interpretation, because there are no known processes that cause a planet’s orbital phase to jump. The dips would then need to be caused by material that was somehow

disrupted from the planet, but somehow remained co-orbital for an extended duration. This seems implausible.

6. CONCLUSIONS

The combination of TESS and Gaia has provided new clarity in the PTFO 8-8695 system. Our main results are as follows.

- *The TESS light-curve shows two periodic signals.* The “long” signal is a 10% peak-to-peak sinusoid that repeats every 11.96 hours. The “short” signal is a 4% peak-to-peak “dip + asymmetric sinusoid” that repeats every 10.74 hours. The signals beat, and therefore cannot be an artifact linked to data processing. Within the angular resolution of the Gaia source catalog, both signals need to originate from PTFO 8-8695.
- *The Gaia data imply binarity.* Relative to stars in its kinematic group, PTFO 8-8695 is a photometric binary (Figure 5, top). Relative to stars in its group that are at least as photometrically variable, PTFO 8-8695 also shows signs of astrometric binarity (Figure 5, bottom).
- *The orbital phase of the dip has changed since the discovery by van Eyken et al. (2012).* As shown in Figure 6, the phase seems to have jumped, perhaps twice. This agrees with the recent study by Tanimoto et al. (2020).
- *All properties of PTFO 8-8695 are consistent with the emerging class of transient and persistent flux dip stars.* Analogous lightcurves are shown in Figure 7. Properties of this variability class are enumerated in Section 5.3.2.

The physical mechanism that explains the transient and persistent flux dips is unresolved. Our preferred explanations include transiting clumps of gas at the Keplerian corotation radius, and occultations of starspots by an optically thick disk (e.g., Stauffer et al. 2017; David et al. 2017; Zhan et al. 2019). The jumping orbital phase disfavors the explanation of an enshrouded, transiting protoplanet. Though PTFO 8-8695b seems unlikely to be a planet, understanding it and its analogs is a worthy problem that promises to teach us about the natal environments of the majority of habitable-zone Earth-sized planets in the Milky Way (Dressing & Charbonneau 2013).

The authors thank D. Fabrycky for helpful tidal evolution calculations that were eventually omitted. PTFO 8-8695 was included on the TESS “short-cadence” target list thanks to the Guest Investigator programs of S. Czesla and C. Huang (G011128 and G011132 respectively). The Digitized Sky Survey was produced at the Space Telescope Science Institute under U.S. Government grant NAG W-2166. Figure 4 is based on photographic data obtained using the Oschin Schmidt Telescope on Palomar Mountain.

Software: astrobases (Bhatti et al. 2018), astropy (Astropy Collaboration et al. 2018), astroquery (Ginsburg et al. 2018), cdips-pipeline (Bhatti et al. 2019)

³ A potential confounding factor is completeness. Is Spitzer sensitive to infrared excesses at the distance of Orion? The series of studies by Hernández et al. (2006, 2007a,b, 2009) show that it is.

corner (Foreman-Mackey 2016), exoplanet (Agol et al. 2019) exoplanet (Foreman-Mackey et al. 2020), and its dependencies (Agol et al. 2019; Kipping 2013; Luger et al. 2019; Theano Development Team 2016). IPython (Pérez & Granger 2007), lightkurve (Lightkurve Collaboration et al. 2018), matplotlib (Hunter 2007), MESA (Paxton et al. 2011, 2013, 2015) numpy (Walt et al. 2011), pandas (McKinney 2010), pyGAM (Servén et al. 2018), PyMC3 (Salvatier et al. 2016), scipy (Jones et al. 2001), tesscut (Brasseur et al. 2019), wotan (Hippke et al. 2019).

Facilities: *Astrometry:* Gaia (Gaia Collaboration et al. 2016, 2018). *Imaging:* Second Generation Digitized Sky Survey, Keck:II (NIRC2; www2.keck.hawaii.edu/inst/nirc2). *Spectroscopy:* Keck:I (HIRES; Vogt et al. 1994). *Photometry:* TESS (Ricker et al. 2015).

Table 1. Model Comparison.

Description	N	M	N_{data}	N_{param}	χ^2	χ^2_{red}	BIC	ΔBIC
Favored	2	2	2585	17	3523.6	1.372	3657.2	0.0
Somewhat favored	2	3	2585	19	3512.7	1.369	3662.0	4.8
Disfavored	3	2	2585	19	3543.1	1.381	3692.4	35.2
—	3	3	2585	21	3536.8	1.379	3701.9	44.6
—	1	2	2585	15	3680.0	1.432	3797.9	140.7
—	1	3	2585	17	3670.2	1.429	3803.8	146.6
—	2	1	2585	15	3700.9	1.440	3818.8	161.6
—	3	1	2585	17	3710.2	1.445	3843.7	186.5
—	1	1	2585	13	3872.7	1.506	3974.8	317.6

NOTE— N and M are the number of harmonics at the short and long periods, respectively. N_{data} is the number of fitted flux measurements. N_{param} is the number of free parameters in the model. The Bayesian information criterion (BIC) and the difference from the maximum ΔBIC are also listed.

Table 2. Best-fit model priors and posteriors.

Param.	Prior	Mean	Std. Dev.	3%	97%
P_s	$\mathcal{N}(0.4485; 0.0010)$	0.4484732	0.0000857	0.4483170	0.4486367
$t_s^{(1)}$	$\mathcal{N}(0.438096; 0.0020)$	0.4384733	0.0017440	0.4349337	0.4415021
R_p/R_*	$\mathcal{N}(0.1100; 0.0033)$	0.11	0.00308	0.10452	0.11599
b	$\mathcal{U}(0; 1 + R_p/R_*)$	0.7736	0.0756	0.6346	0.8993
u_1	(2)	0.683	0.477	0.001	1.546
u_2	(2)	0.004	0.417	-0.793	0.727
Mean	$\mathcal{U}(-0.01; 0.01)$	-0.000885	0.000440	-0.001745	-0.000088
ω_s	$2\pi/P_s$	14.01017	0.00268	14.00506	14.01505
$A_{s,0}$	$\mathcal{U}(-0.02; 0.02)$	0.008903	0.000705	0.007569	0.010277
$B_{s,0}$	$\mathcal{U}(-0.02; 0.02)$	0.009985	0.000751	0.008504	0.011289
$A_{s,1}$	$\mathcal{U}(-0.02; 0.02)$	0.001649	0.000696	0.000331	0.002884

Table 2 continued

Table 2 (*continued*)

Param.	Prior	Mean	Std. Dev.	3%	97%
$B_{s,1}$	$\mathcal{U}(-0.02; 0.02)$	-0.005267	0.000606	-0.006491	-0.004203
ϕ_ℓ	$\mathcal{U}(1.3721; 2.1575)$	1.74324	0.22254	1.38274	2.08874
ω_ℓ	$\mathcal{N}(12.6054; 0.1261)$	12.588581	0.002040	12.584940	12.592450
$A_{\ell,0}$	$\mathcal{U}(-0.06; 0.06)$	0.037785	0.005150	0.028728	0.045214
$B_{\ell,0}$	$\mathcal{U}(-0.06; 0.06)$	0.022288	0.008592	0.008066	0.0359
$A_{\ell,1}$	$\mathcal{U}(-0.02; 0.02)$	0.002326	0.000756	0.000857	0.003658
$B_{\ell,1}$	$\mathcal{U}(-0.02; 0.02)$	-0.002197	0.000744	-0.003512	-0.000743

(1) To convert mean TESS mid-transit time to BJD_{TDB} , add 2458468.2. (2) Quadratic limb-darkening prior from [Kipping \(2013\)](#), implemented by [Foreman-Mackey et al. \(2020\)](#).

REFERENCES

- Agol, E., Luger, R., & Foreman-Mackey, D. 2019, [arXiv e-prints, 1908.03222](#)
- Ansdell, M., Gaidos, E., Rappaport, S. A., et al. 2016, [ApJ](#), **816**, 69
- Astropy Collaboration, Price-Whelan, A. M., Sipőcz, B. M., et al. 2018, [AJ](#), **156**, 123
- Barnes, J. W., van Eyken, J. C., Jackson, B. K., Ciardi, D. R., & Fortney, J. J. 2013, [ApJ](#), **774**, 53
- Belokurov, V., Penoyre, Z., Oh, S., et al. 2020, [arXiv:2003.05467 \[astro-ph\]](#), arXiv: 2003.05467
- Bhatti, W., Bouma, L., & Yee, S. 2019, `cdips-pipeline` v0.1.0, <https://doi.org/10.5281/zenodo.3370324>
- Bhatti, W., Bouma, L. G., & Wallace, J. 2018, `astrobase`, <https://doi.org/10.5281/zenodo.1469822>
- Blanton, M. R., Bershadsky, M. A., Abolfathi, B., et al. 2017, [AJ](#), **154**, 28
- Bouma, L. G., Hartman, J. D., Bhatti, W., Winn, J. N., & Bakos, G. Á. 2019, [ApJS](#), **245**, 13
- Brasseur, C. E., Phillip, C., Fleming, S. W., Mullally, S. E., & White, R. L. 2019, [Astrophysics Source Code Library](#), [ascl:1905.007](#)
- Briceño, C., Calvet, N., Hernández, J., et al. 2005, [AJ](#), **129**, 907
- Briceño, C., Hartmann, L., Hernández, J., et al. 2007a, [ApJ](#), **661**, 1119
- Briceño, C., Preibisch, T., Sherry, W. H., et al. 2007b, [Protostars and Planets V](#), 345
- Briceño, C., Calvet, N., Hernández, J., et al. 2019, [AJ](#), **157**, 85
- Ciardi, D. R., Eyken, J. C. v., Barnes, J. W., et al. 2015, [ApJ](#), **809**, 42, publisher: IOP Publishing
- Cody, A. M., & Hillenbrand, L. A. 2018, [AJ](#), **156**, 71
- Cottle, J., Covey, K. R., Suárez, G., et al. 2018, [ApJS](#), **236**, 27
- Cropper, M., Katz, D., Sartoretti, P., et al. 2018, [A&A](#), **616**, A5
- David, T. J., Petigura, E. A., Hillenbrand, L. A., et al. 2017, [ApJ](#), **835**, 168
- Dressing, C. D., & Charbonneau, D. 2013, [ApJ](#), **767**, 95
- Duchêne, G., & Kraus, A. 2013, [ARA&A](#), **51**, 269
- Evans, D. W., Riello, M., De Angeli, F., et al. 2018, [A&A](#), **616**, A4
- Foreman-Mackey, D. 2016, [The Journal of Open Source Software](#), **24**
- Foreman-Mackey, D., Czekala, I., Luger, R., et al. 2020, `exoplanet-dev/exoplanet` v0.2.6
- Gaia Collaboration, Prusti, T., de Bruijne, J. H. J., et al. 2016, [A&A](#), **595**, A1
- Gaia Collaboration, Brown, A. G. A., Vallenari, A., et al. 2018, [A&A](#), **616**, A1
- Gelman, A., & Rubin, D. B. 1992, [Statistical Science](#), **7**, 457, publisher: Institute of Mathematical Statistics
- Ginsburg, A., Sipocz, B., Madhura Parikh, et al. 2018, `Astropy/Astroquery: V0.3.7 Release`
- Gunn, J. E., Siegmund, W. A., Mannery, E. J., et al. 2006, [AJ](#), **131**, 2332
- Henry, T. J., Jao, W.-C., Subasavage, J. P., et al. 2006, [AJ](#), **132**, 2360
- Hernández, J., Briceño, C., Calvet, N., et al. 2006, [ApJ](#), **652**, 472
- Hernández, J., Calvet, N., Hartmann, L., et al. 2009, [ApJ](#), **707**, 705
- Hernández, J., Calvet, N., Briceño, C., et al. 2007a, [ApJ](#), **671**, 1784
- Hernández, J., Hartmann, L., Megeath, T., et al. 2007b, [ApJ](#), **662**, 1067
- Hipke, M., David, T. J., Mulders, G. D., & Heller, R. 2019, [arXiv:1906.00966 \[astro-ph\]](#), arXiv: 1906.00966
- Hoffman, M. D., & Gelman, A. 2014, [Journal of Machine Learning Research](#), **15**, 1593
- Howarth, I. D. 2016, [MNRAS](#), **457**, 3769
- Howell, S. B., Sobeck, C., Haas, M., et al. 2014, [PASP](#), **126**, 398

- Hunter, J. D. 2007, *Computing in Science & Engineering*, 9, 90
- Jeffries, R. D., Maxted, P. F. L., Oliveira, J. M., & Naylor, T. 2006, *MNRAS*, 371, L6
- Jenkins, J. M., Twicken, J. D., McCaulliff, S., et al. 2016, *Software and Cyberinfrastructure for Astronomy IV*, 9913, 99133E
- Johns-Krull, C. M., Prato, L., McLane, J. N., et al. 2016, *ApJ*, 830, 15
- Jones, E., Oliphant, T., Peterson, P., et al. 2001, Open source scientific tools for Python
- Kamiaka, S., Masuda, K., Xue, Y., et al. 2015, *Publications of the Astronomical Society of Japan*, 67, 94
- Kipping, D. M. 2013, *MNRAS*, 435, 2152
- Koen, C. 2015, *MNRAS*, 450, 3991
- Kounkel, M., Covey, K., Suárez, G., et al. 2018, *AJ*, 156, 84
- Kraus, A. L., Ireland, M. J., Huber, D., Mann, A. W., & Dupuy, T. J. 2016, *AJ*, 152, 8
- Kraus, A. L., Ireland, M. J., Martinache, F., & Hillenbrand, L. A. 2011, *ApJ*, 731, 8
- Kraus, A. L., Ireland, M. J., Martinache, F., & Lloyd, J. P. 2008, *ApJ*, 679, 762
- Lee, C.-H., & Chiang, P.-S. 2018, *ApJL*, 852, L24
- Lightkurve Collaboration, Cardoso, J. V. d. M., Hedges, C., et al. 2018, Lightkurve: Kepler and TESS time series analysis in Python, Astrophysics Source Code Library, [ascl:1812.013](#)
- Lindgren, L., Hernández, J., Bombrun, A., et al. 2018, *Astronomy & Astrophysics*, 616, A2
- Lomb, N. R. 1976, *Astrophysics and Space Science*, 39, 447
- Luger, R., Agol, E., Foreman-Mackey, D., et al. 2019, *AJ*, 157, 64
- Luger, R., Agol, E., Kruse, E., et al. 2016, *AJ*, 152, 100
- Luger, R., Bedell, M., Vanderspek, R., & Burke, C. J. 2019, [arXiv:1903.12182 \[astro-ph\]](#), arXiv: 1903.12182
- Luger, R., Kruse, E., Foreman-Mackey, D., Agol, E., & Saunders, N. 2018, *AJ*, 156, 99
- Majewski, S. R., Schiavon, R. P., Frinchaboy, P. M., et al. 2017, *AJ*, 154, 94
- McKinney, W. 2010, in *Proceedings of the 9th Python in Science Conference*, ed. S. van der Walt & J. Millman, 51
- Moe, M., & Kratter, K. M. 2019, [arXiv:1912.01699 \[astro-ph\]](#), arXiv: 1912.01699
- Onitsuka, M., Fukui, A., Narita, N., et al. 2017, *Publications of the Astronomical Society of Japan*, 69
- Paxton, B., Bildsten, L., Dotter, A., et al. 2011, *ApJS*, 192, 3
- Paxton, B., Cantiello, M., Arras, P., et al. 2013, *ApJS*, 208, 4
- Paxton, B., Marchant, P., Schwab, J., et al. 2015, *ApJS*, 220, 15
- Pérez, F., & Granger, B. E. 2007, *Computing in Science and Engineering*, 9, 21
- Raetz, S., Schmidt, T. O. B., Czesla, S., et al. 2016, *MNRAS*, 460, 2834
- Rebull, L. M., Stauffer, J. R., Cody, A. M., et al. 2020
- . 2018, *AJ*, 155, 196
- Rebull, L. M., Stauffer, J. R., Bouvier, J., et al. 2016, *AJ*, 152, 114
- Ricker, G. R., Winn, J. N., Vanderspek, R., et al. 2015, *Journal of Astronomical Telescopes, Instruments, and Systems*, 1, 014003
- Rizzuto, A. C., Vanderburg, A., Mann, A. W., et al. 2018, [arXiv:1808.07068 \[astro-ph\]](#), arXiv: 1808.07068
- Salvatier, J., Wiecki, T. V., & Fonnesbeck, C. 2016, PyMC3: Python probabilistic programming framework
- Scargle, J. D. 1982, *ApJ*, 263, 835
- Schmidt, T. O. B., Neuhauser, R., Briceño, C., et al. 2016, *A&A*, 593, A75
- Servén, D., Brummitt, C., & Abedi, H. 2018, *dswah/pyGAM*: v0.8.0
- Shporer, A. 2017, *PASP*, 129, 072001
- Smith, J. C., Morris, R. L., Jenkins, J. M., et al. 2017a, *Kepler Science Document*, 7
- Smith, J. C., Stumpe, M. C., Jenkins, J. M., et al. 2017b, *Kepler Science Document*, 8
- Stassun, K. G., Oelkers, R. J., Pepper, J., et al. 2018, *AJ*, 156, 102
- Stassun, K. G., Oelkers, R. J., Paegert, M., et al. 2019, [arXiv:1905.10694 \[astro-ph\]](#), arXiv: 1905.10694
- Stauffer, J., Rebull, L. M., Cody, A. M., et al. 2018, *AJ*, 156, 275, publisher: American Astronomical Society
- Stauffer, J., Cameron, A. C., Jardine, M., et al. 2017, *AJ*, 153, 152
- Tanimoto, Y., Yamashita, T., Ui, T., et al. 2020, *PASJ*, [arXiv:2001.00148 \[astro-ph.EP\]](#)
- Tenenbaum, P., & Jenkins, J. 2018, TESS Science Data Products Description Document, EXP-TESS-ARC-ICD-0014 Rev D, <https://archive.stsci.edu/missions/tess/doc/EXP-TESS-ARC-ICD-TM-0014.pdf>
- Theano Development Team. 2016, [arXiv e-prints](#), [abs/1605.02688](#)
- van Eyken, J. C., Ciardi, D. R., von Braun, K., et al. 2012, *ApJ*, 755, 42
- VanderPlas, J. T., & Ivezić, Z. 2015, *ApJ*, 812, 18
- Vogt, S. S., Allen, S. L., Bigelow, B. C., et al. 1994, SPIE Conference Series, ed. D. L. Crawford & E. R. Craine, Vol. 2198
- Walt, S. v. d., Colbert, S. C., & Varoquaux, G. 2011, *Computing in Science & Engineering*, 13, 22
- Winn, J. N. 2010, *Exoplanet Transits and Occultations*, ed. S. Seager, 55
- Yu, L., Winn, J. N., Gillon, M., et al. 2015, *ApJ*, 812, 48
- Zasowski, G., Cohen, R. E., Chojnowski, S. D., et al. 2017, *AJ*, 154, 198
- Zhan, Z., Günther, M. N., Rappaport, S., et al. 2019, *ApJ*, 876, 127
- Ziegler, C., Law, N. M., Baranec, C., et al. 2018, [arXiv:1806.10142 \[astro-ph\]](#), arXiv: 1806.10142